

## Article

# Metalloporphyrin-Based Metal–Organic Frameworks for Photocatalytic Carbon Dioxide Reduction: The Influence of Metal Centers

Qian Li, Keke Wang \* , Heyu Wang, Mengmeng Zhou, Bolin Zhou, Yanzhe Li, Qiang Li, Qin Wang, Hai-Min Shen and Yuanbin She \*

State Key Laboratory Breeding Base of Green Chemistry–Synthesis Technology, College of Chemical Engineering, Zhejiang University of Technology, Hangzhou 310014, China

\* Correspondence: wangkk@zjut.edu.cn (K.W.); sheyb@zjut.edu.cn (Y.S.)

**Abstract:** Photocatalysis is one of the most promising technologies to achieve efficient carbon dioxide reduction reaction (CO<sub>2</sub>RR) under mild conditions. Herein, metalloporphyrin-based metal–organic frameworks (MOFs) with different metal centers, denoted as PCN-222, were utilized as visible-light photocatalysts for CO<sub>2</sub> reduction. Due to the combination of the conjugated planar macrocyclic structures of metalloporphyrins and the stable porous structures of MOFs, all PCN-222 materials exhibited excellent light-harvesting and CO<sub>2</sub>-adsorbing abilities. Among the studied MOFs of varied metal centers (M = Pt, Fe, Cu, Zn, Mn), PCN-222(2H&Zn) exhibited the highest photocatalytic CO<sub>2</sub>RR performance, with an average CO yield of 3.92 μmol g<sup>−1</sup> h<sup>−1</sup> without any organic solvent or sacrificial agent. Furthermore, this was three and seven times higher than that of PCN-222(Zn) (1.36 μmol g<sup>−1</sup> h<sup>−1</sup>) and PCN-222(2H) (0.557 μmol g<sup>−1</sup> h<sup>−1</sup>). The superior photocatalytic activity of PCN-222(2H&Zn) was attributed to its effective photoexcited electron–hole separation and transportation compared with other PCN-222(2H&M) materials. The obtained results indicate that Zn ions in the porphyrin’s center played an important role in the reaction of active sites for the adsorption–activation of CO<sub>2</sub>. In addition, PCN-222(2H&Zn) showed the highest CO<sub>2</sub> selectivity (almost 100%) and stability. This work provides a clear guide for the design of efficient photocatalysts.

**Keywords:** metalloporphyrin; metal–organic frameworks; PCN-222; photocatalysis; carbon dioxide reduction



**Citation:** Li, Q.; Wang, K.; Wang, H.; Zhou, M.; Zhou, B.; Li, Y.; Li, Q.; Wang, Q.; Shen, H.-M.; She, Y. Metalloporphyrin-Based Metal–Organic Frameworks for Photocatalytic Carbon Dioxide Reduction: The Influence of Metal Centers. *Processes* **2023**, *11*, 1042. <https://doi.org/10.3390/pr11041042>

Academic Editors: Kejun Wu, An Su and Maria Victoria Lopez-Ramon

Received: 16 February 2023

Revised: 17 March 2023

Accepted: 25 March 2023

Published: 30 March 2023



**Copyright:** © 2023 by the authors. Licensee MDPI, Basel, Switzerland. This article is an open access article distributed under the terms and conditions of the Creative Commons Attribution (CC BY) license (<https://creativecommons.org/licenses/by/4.0/>).

## 1. Introduction

Climate change is caused by the gradual increase in atmospheric CO<sub>2</sub> concentration and has become a significant global problem, which seriously threatens the Earth’s living systems [1,2]. However, CO<sub>2</sub> is also a cheap and easily available green C1 resource. The efficient conversion of CO<sub>2</sub> into high-value-added fine chemical materials and energy fuels (e.g., CO, CH<sub>4</sub>, HCOOH, and CH<sub>3</sub>OH) not only helps to solve environmental problems and energy crises but also obeys the sustainable development guidelines [3]. To date, the main pathways for CO<sub>2</sub> conversion include thermocatalysis [4], photocatalysis [5], electrocatalysis [6], and biocatalysis [7]. Among these methods, the photocatalytic CO<sub>2</sub> reduction process simulates natural photosynthesis by using solar energy and photocatalysts to achieve the catalytic conversion of CO<sub>2</sub> and H<sub>2</sub>O. Moreover, photocatalysis exhibits the following three advantages: (1) unlimited solar energy, (2) mild reaction conditions, and (3) no secondary pollution [8–10]. These superiorities make it a promising strategy for CO<sub>2</sub> reduction. However, the conversion efficiency of photocatalytic CO<sub>2</sub> reduction and its selectivity towards target products should be further improved by developing efficient catalysts.

Porphyrin molecules are conjugated cyclic structures with π electrons, leading to the fluidity of electrons in the molecular rings. Furthermore, the majority of porphyrins and

their derivatives have obvious optical properties [11–13]. Under light conditions, porphyrin compounds absorb light excitation to produce electrons. Inspired by photosynthesis, porphyrins and their derivatives are usually used as photosensitizers for the photocatalytic degradation of pollutants [14], hydrogen production [15], carbon dioxide reduction [16], and so on. Moreover, the porous structure consisting of metalloporphyrin monomer materials benefits the adsorption and activation of CO<sub>2</sub> on the surface of porphyrin materials. However, due to porphyrins being a homogeneous catalyst, they are not conducive to recovery and cannot be recycled; hence, the self-assembled materials of porphyrins have attracted wide attention. Recently, metal–organic framework materials (MOFs) have attracted considerable attention as a new type of porous material [17–19]. Taking advantage of their large specific surface area, regular porous channels, and adjustable pore size, MOFs are considered promising materials for trapping and storing CO<sub>2</sub> molecules, as well as enhancing the stability of catalysts [20–22]. Thus, the well-organized assembly of metalloporphyrin-based MOFs can effectively modulate the photo-response range and improve the adsorption–activation ability of CO<sub>2</sub> during CO<sub>2</sub> reduction [23,24], which further enhances the photocatalytic CO<sub>2</sub> reduction performance. To date, metalloporphyrin-based MOFs have been used in the photocatalytic reduction of CO<sub>2</sub> and exhibit significant photocatalytic activity for this purpose. For example, PCN-222 (no metal) promoted the photocatalytic conversion of CO<sub>2</sub> into a formate anion [25]. However, the photocatalytic reduction of CO<sub>2</sub> over metalloporphyrin-based MOFs was mainly conducted with TEOA in CH<sub>3</sub>CN as a sacrificial agent and solvent, respectively. The harsh reaction conditions may lead to environmental pollution and high cost. It is worth noting that, in the absence of any organic solvents and sacrificial agents, only a few catalysts have been reported for the reduction of CO<sub>2</sub> in water. In addition, the effect of metals in metalloporphyrin on CO<sub>2</sub> reduction activity in water has rarely been examined. Therefore, due to its excellent chemical stability, Zr-based PCN-222 was selected as a photocatalytic CO<sub>2</sub> reduction catalyst for our study, where the effect of various metal ions on porphyrin was investigated.

Herein, the metalloporphyrin-based MOFs, denoted as PCN-222(2H&M) (M = Pt, Fe, Cu, Zn, and Mn), were prepared via the hydrothermal process. PCN-222 materials were used as photocatalysts for CO<sub>2</sub> reduction in water without any organic solvent or sacrificial agent. The effects of the five central metals of porphyrins on the photocatalytic reaction were systematically investigated, and their activation centers and mechanisms were discussed. The photocatalytic tests demonstrated that PCN-222(2H&Zn) showed the highest CO<sub>2</sub> conversion into CO among the materials studied. This was attributed to PCN-222(2H&Zn) exhibiting the most effective photoexcited electron–hole separation and transportation. Hence, PCN-222(2H&Zn) has broad application prospects in photocatalytic CO<sub>2</sub> reduction in the future.

## 2. Materials and Methods

### 2.1. Materials

Pyrrole (C<sub>4</sub>H<sub>5</sub>N, 99.0%), methyl *p*-formylbenzoate (C<sub>9</sub>H<sub>8</sub>O<sub>3</sub>, 99.0%), and propionic acid (C<sub>3</sub>H<sub>4</sub>O<sub>2</sub>, 99.0%) were purchased from DAMAS-Beta. Zinc (II) acetate dihydrate (Zn(CH<sub>3</sub>COO)<sub>2</sub>·2H<sub>2</sub>O, 98%), copper (II) acetate monohydrate ((CH<sub>3</sub>COO)<sub>2</sub>Cu·H<sub>2</sub>O, 98%), manganese acetate tetrahydrate (II) ((CH<sub>3</sub>COO)<sub>2</sub>Mn·4H<sub>2</sub>O, 99%), iron (II) chloride tetrahydrate (FeCl<sub>2</sub>·4H<sub>2</sub>O, 98%), platinum (II) dichloride (PtCl<sub>2</sub>, 98%), zirconium (IV) chloride (ZrCl<sub>4</sub>, 98%), and formic acid (HCOOH, 98%) were purchased from Sinopharm Chemical Reagent Co., Ltd. (Shanghai, China). All reagents were analytically pure and used without any further purification, except for pyrrole.

### 2.2. Synthesis of PCN-222(2H), PCN-222(Zn), and PCN-222(2H&M)

*meso*-Tetra(4-carboxyphenyl)porphine (H<sub>2</sub>TCPP) and M(Pt(II), Fe(III), Cu(II), Zn(II), and Mn(II))-*meso*-tetra(4-carboxyphenyl)porphine (TCPP-M) were synthesized following a previously described procedure [19,20]. In the synthesis of PCN-222(2H), 42 mg zirconium tetra-chloride (ZrCl<sub>4</sub>) was added to *N,N*-dimethylformamide (DMF, 20 mL) and stirred

for 30 min. Then, 60 mg H<sub>2</sub>TCPP (0.04 mmol) was added to the solution. After 10 min of stirring, formic acid (5 mL) was added. The solution was heated to 120 °C for 16 h in a 100 mL thick-walled pressure-resistant flask. After cooling to room temperature, the generated precipitate was collected by centrifugation, washed repeatedly using DMF and acetone, and dried under vacuum at 80 °C.

The synthesis of PCN-222(Zn) was performed under the same conditions except that 64.8 mg TCPP-Zn (0.08 mmol) was added.

The synthesis of PCN-222(2H&M) was performed under the same conditions except that H<sub>2</sub>TCPP (0.04 mmol) and TCPP-M (0.04 mmol) were added.

### 2.3. Characterizations

Powder X-ray diffraction (PXRD) was performed using a Rigaku D/Max-2400/PC with diffraction angles from 2° to 30°. Fourier transform infrared (FT-IR) spectra were recorded using a Nicolet NEXUS 670 spectrometer (United States Thermo Fisher Scientific). The morphologies of the obtained MOFs were characterized using a Hitachi S-4700 Field Emission scanning electron microscope (SEM) with Energy-dispersive X-ray (EDX) spectrometer. The Quantachrome Autosorb-iQ automated gas adsorption system was used to detect N<sub>2</sub> adsorption/desorption isotherms and BET-specific surface area. Thermal gravimetric analysis (TGA) was carried out using a NETZSCH STA 449 instrument at a heating rate of 10 °C min<sup>-1</sup> under an air atmosphere. Ultraviolet–visible (UV–vis) absorption was tested using a Cary 5000 UV–vis–NIR spectrometer with BaSO<sub>4</sub> as a standard reference. The isotope-labeled experiment was conducted using <sup>13</sup>CO<sub>2</sub> instead of <sup>12</sup>CO<sub>2</sub>, and the products were analyzed by gas chromatography–mass spectrometry (7890A and 5975C, Agilent). CO<sub>2</sub> TPD measurements were carried out using a quantachrome autosorb-iQ-C chemisorption analyzer with a thermal conductivity detector. Photoluminescence (PL) was detected using a fluorescence lifetime spectrometer (FLS980-D2S2-STM). Electron paramagnetic resonance (EPR) spectra were obtained using a JEOL JES-FA200 ESR spectrometer at 77 K.

### 2.4. Photoelectrochemical Performance

The photoelectrochemical performance measurements were performed using a CHI660E electrochemical workstation. The electrochemical impedance spectroscopy (EIS) was performed using carbon cloth as the working electrode, Ag/AgCl as the reference electrode, and platinum electrode as the counter electrode. A 0.1 M KCl solution containing 5 mM Fe(CN)<sub>6</sub><sup>3-</sup> was used as the electrolyte. The Mott-Schottky (M-S) curve test was conducted using the glassy carbon electrode as the working electrode, Ag/AgCl as the reference electrode, platinum plate as the counter electrode, and 0.5 M sodium sulfate solution as the electrolyte. In the case of the photocurrent test, FOT acted as the working electrode, Ag/AgCl as the reference electrode, platinum plate as the counter electrode, and 0.5 M sodium sulfate solution as the electrolyte.

### 2.5. Photocatalytic Activity

The photocatalytic CO<sub>2</sub> reduction was carried out using the all-glass automates' on-line trace gas analysis system (Beijing Perfectlight Technology Co., Ltd. (Beijing, China). Labsolar-6A). After accurately weighing 30 mg catalyst, 50 mL water was measured and added to the all-glass reactor. After connecting the reactor to the system, the circulating cooling water pump system was automatically started, the reactor was sealed, the vacuum pump was started, and high-purity CO<sub>2</sub> gas was introduced into the reactor, while the pressure inside was maintained at 80 KPa. To reduce experimental error and ensure that the CO<sub>2</sub>-filled air was completely removed from the reactor, this step was repeated three times. The photocatalytic activity of the prepared samples was evaluated by CO<sub>2</sub> reduction in simulated sunlight, using a 300 W xenon lamp (Beijing Perfectlight Technology Co., Ltd. (Beijing, China). PLS-SXE300D) as the all-light source.

### 3. Results and Discussion

#### 3.1. Characterization of Catalysts

The crystal structures of all prepared PCN-222 materials were investigated using PXRD. As shown in Figure 1a, the Bragg diffraction peaks of the above samples at  $2\theta = 2.4, 4.9, 6.6, 7.1,$  and  $9.9^\circ$  represented their (100), (200), (2–11), (201), and (4–21) crystal facets, respectively. This was consistent with the simulated patterns of PCN-222 [26,27]. The results show that the crystal structure of PCN-222 was fully preserved and well-defined during the formation of PCN-222(2H&M). FT-IR spectroscopy of all PCN-222 materials is shown in Figure 1b. The peaks at  $475\text{ cm}^{-1}$  were attributed to Zr-O stretch, indicating the coordination between -COOH and  $\text{Zr}^{4+}$  of PCN-222 [28]. Compared with PCN-222(2H), all PCN-222(2H&M) materials exhibited a new peak at ca.  $1000\text{ cm}^{-1}$ , which was attributed to the strong M-N bond stretch of metalloporphyrin [27,29–31]. The surface morphologies of PCN-222 materials were observed by SEM, which exhibited rodlike structures (Figure 1c–h). Importantly, PCN-222(Zn) showed the smallest nanoscale dimension of ca.  $\sim 75.9\text{ nm}$  compared with that of other PCN-222 materials (PCN-222(2H):  $5.78\text{ }\mu\text{m}$ , PCN-222(2H&Pt):  $3.73\text{ }\mu\text{m}$ , PCN-222(2H&Fe):  $94\text{ nm}$ , PCN-222(2H&Cu):  $1.25\text{ }\mu\text{m}$ , and PCN-222(2H&Mn):  $121.3\text{ nm}$ ). EDX-mapping images showed the uniform distribution of C, N, O, and Zr in all PCN-222 (Supporting Information, Figure S1). Moreover, the Pt, Mn, Fe, Cu, and Zn elements were found in the corresponding PCN-222(2H&M) materials, respectively.

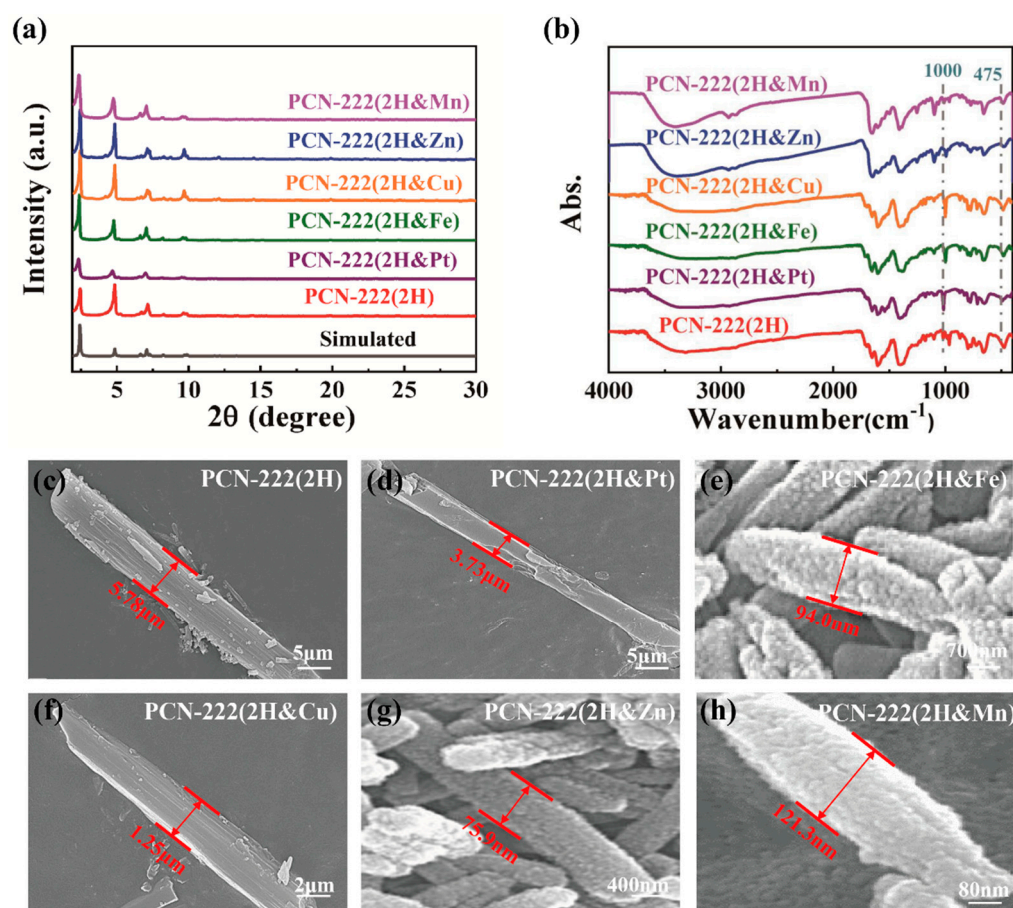


**Figure 1.** (a) PXRD patterns, (b) FT-IR spectra of all materials, and (c–h) scanning electron microscopy (SEM) images of (c) PCN-222(2H), (d) PCN-222(2H&Pt), (e) PCN-222(2H&Fe), (f) PCN-222(2H&Cu), (g) PCN-222(2H&Zn), and (h) PCN-222(2H&Mn).

The surface chemical composition and valence states of all PCN-222 materials were measured by XPS. XPS spectra of PCN-222(2H&M) showed the presence of C, O, N, Zr, and various

metal elements in the porphyrin's center (Figure 2a). Pt 4f spectrum (Figure 2b) displayed two peaks at ca. 73.3 eV and 76.4 eV that represented Pt 4f<sub>7/2</sub> and Pt 4f<sub>5/2</sub> and indicated the presence of the oxidation state of Pt(II) of PCN-222(2H&Pt) [32]. As shown in Figure 2c, Fe 2p spectrum was deconvoluted into two peaks at the binding energy of 710.9 eV (Fe 2p<sub>3/2</sub>) and 724.1 eV (Fe 2p<sub>1/2</sub>), existing in PCN-222(2H&Fe) as Fe(III) state [33,34]. As shown in Figure 2d, Cu 2p<sub>3/2</sub> and Cu 2p<sub>1/2</sub> peaks appeared at ca. 934.9 eV and 954.8 eV. Additionally, the two strong satellite peaks at 943.0 eV and 963.2 eV were attributed to Cu(II) state of PCN-222(2H&Cu). The two intense peaks at 1044.9 eV (Zn 2p<sub>1/2</sub>) and 1021.7 eV (Zn 2p<sub>3/2</sub>) were observed in the Zn 2p spectrum (Figure 2e) and were related to Zn-N in the Zn(II) state of PCN-222(2H&Zn) [35]. Mn 2p spin-orbit doublet peaks appeared at ca. 653.0 eV (Mn 2p<sub>1/2</sub>) and 641.4 eV (Mn 2p<sub>3/2</sub>) in Figure 2f, and the unique satellite peak at 644.7 eV was attributed to Mn(II) of PCN-222(2H&Mn) [36]. Therefore, the above results verify the successful incorporation and valence states of various metal ions in PCN-222(2H&M).

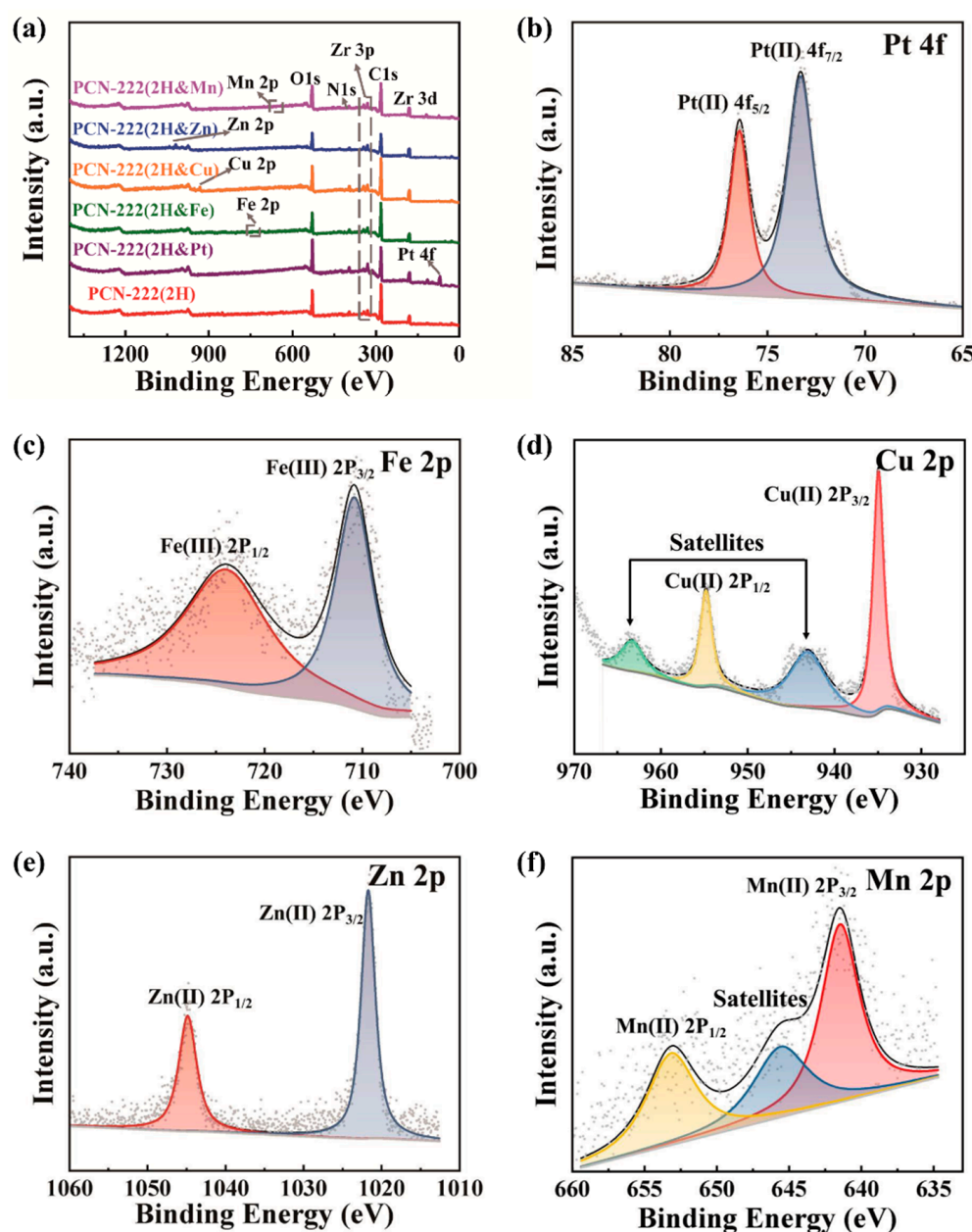


**Figure 2.** (a–f) XPS spectra: (a) survey of PCN-222 materials, (b) Pt 4f of PCN-222(2H&Pt), (c) Fe 2p of PCN-222(2H&Fe), (d) Cu 2p of PCN-222(2H&Cu), (e) Zn 2p of PCN-222(2H&Zn), and (f) Mn 2p of PCN-222(2H&Mn).

In Figure 3a, PCN-222(2H) and PCN-222(2H&M) exhibited type IV adsorption/desorption isotherms with obvious hysteresis loops at the relative pressure from 0.4 to 1.0 in the desorption branches. Based on the Brunauer–Emmett–Teller (BET) method, the specific surface area (SSA) of PCN-222(2H) was  $1553 \text{ m}^2 \text{ g}^{-1}$ , and the SSAs of PCN-222(2H&Pt), PCN-222(2H&Mn), PCN-222(2H&Fe), PCN-222(2H&Cu), and PCN-222(2H&Zn) were 1126, 1024, 1071, 1249, and  $1350 \text{ m}^2 \text{ g}^{-1}$ , respectively (Supporting Information, Table S1). Compared with PCN-222(2H), the decrease in SSAs of PCN-222(2H&M) was ascribed to the introduction of metal sites in the porphyrin's center [37]. Furthermore, SSA and the total pore volume ( $0.85 \text{ cm}^3 \text{ g}^{-1}$ ) of PCN-222(2H&Zn) were the highest among the other PCN-222(2H&M) materials. In addition, the pore size distribution of PCN-222(2H) and PCN-222(2H&M) exhibited hierarchically porous structures (0.5–1 nm and 2–4 nm). As a result, high SSA and abundant micro/mesopores of PCN-222(2H&Zn) ensured the exposed active sites of  $\text{CO}_2$  adsorption and promoted the proximity of target reactants to the active sites, which benefited the photocatalytic reduction of  $\text{CO}_2$  [38]. As shown in Figure S2 (Supporting Information), under an air atmosphere, the thermal degradation of PCN-222 materials occurred at ca.  $390^\circ\text{C}$ . The introduction of metal ions did not affect their thermal stability.

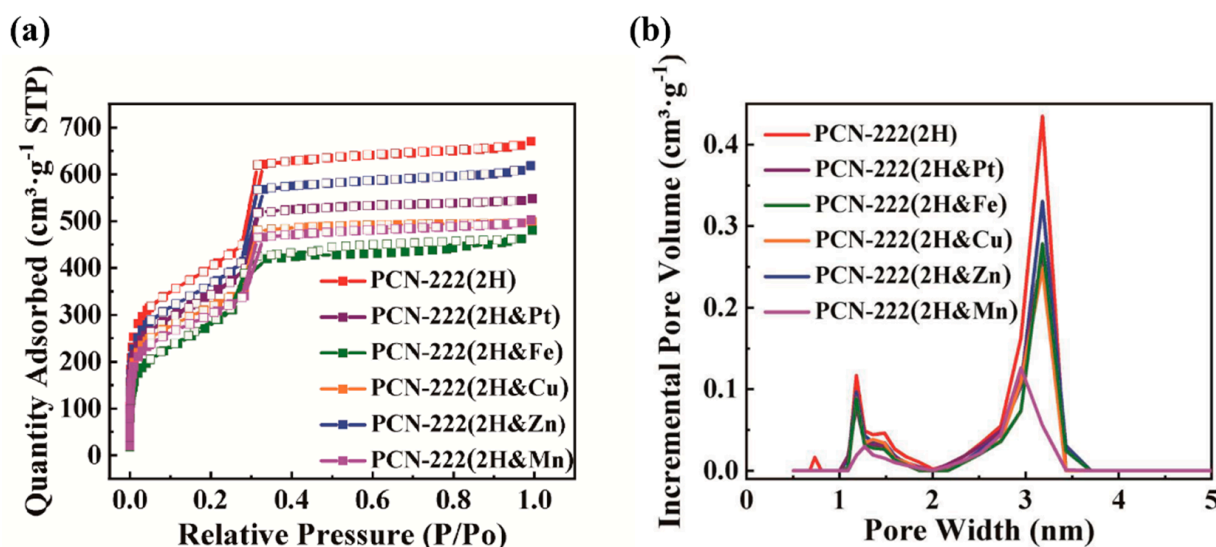


**Figure 3.** (a) Nitrogen adsorption/desorption isotherms of PCN-222 materials at 77 K (adsorption is marked by filled squares; desorption is marked by empty squares) and (b) pore size distribution of PCN-222(2H) and PCN-222(2H&M).

The UV–vis spectra of PCN-222(2H) and PCN-222(2H&M) exhibited a broad and strong absorption band in the region of 200–800 nm, which was consistent with a porphyrin ligand, making them suitable for photoreduction applications (Figure 4a and Supporting information, Figure S3). The UV–vis diffuse reflectance spectrum (Figure 4a) shows that PCN-222(2H&Zn) had an energy bandgap of 1.95 eV by intercepting  $(Ah\nu)^2$  and the tangent to the photon energy. In order to elucidate the semiconductor properties of PCN-222(2H&M) and the possibility of subsequent  $\text{CO}_2$  photoreduction, Mott–Schottky (M-S) measurements on PCN-222(2H&M) photoanode were conducted at frequencies of 500, 1000 and 1500 Hz, respectively (Supporting information, Figure S3). The potential position of PCN-222(2H&Zn) was calculated by M-S curves (Figure 4b). The positive slope indicated that the rod-shaped PCN-222(2H&Zn) was an n-type semiconductor, and the conduction band minimum (CBM) was determined from the flat band potential ( $E_{fb}$ ). Compared with Ag/AgCl and normal hydrogen electrode (NHE), the  $E_{fb}$  of PCN-222(2H&Zn) under pH = 7 were ca.  $-0.53 \text{ eV}$  and  $-0.33 \text{ eV}$ , respectively. Due to  $E_{fb}$  generally being  $\sim 0.2 \text{ V}$  below the CBM in n-type semiconductors, the CBM of PCN-222(2H&Zn) was  $-0.53 \text{ eV}$  vs. NHE [39,40]. Furthermore, the valence band maximum (VBM) of PCN-222(2H&Zn)

was estimated as +1.42 eV vs. NHE in comparison with the band gap. The CBM and VBM positions of PCN-222(2H) and PCN-222(2H&M) are presented in Figure 4c. It can be found that the CBM (VBM) positions of all PCN-222 materials were more negative (positive) than the redox potentials of CO<sub>2</sub>/CO (O<sub>2</sub>/H<sub>2</sub>O). Based on the results of the as-calculated energy band alignments, PCN-222(2H&Zn) exhibits an ideal thermodynamic driving force and electron reduction capability for the overall CO<sub>2</sub> reduction in a H<sub>2</sub>O medium.

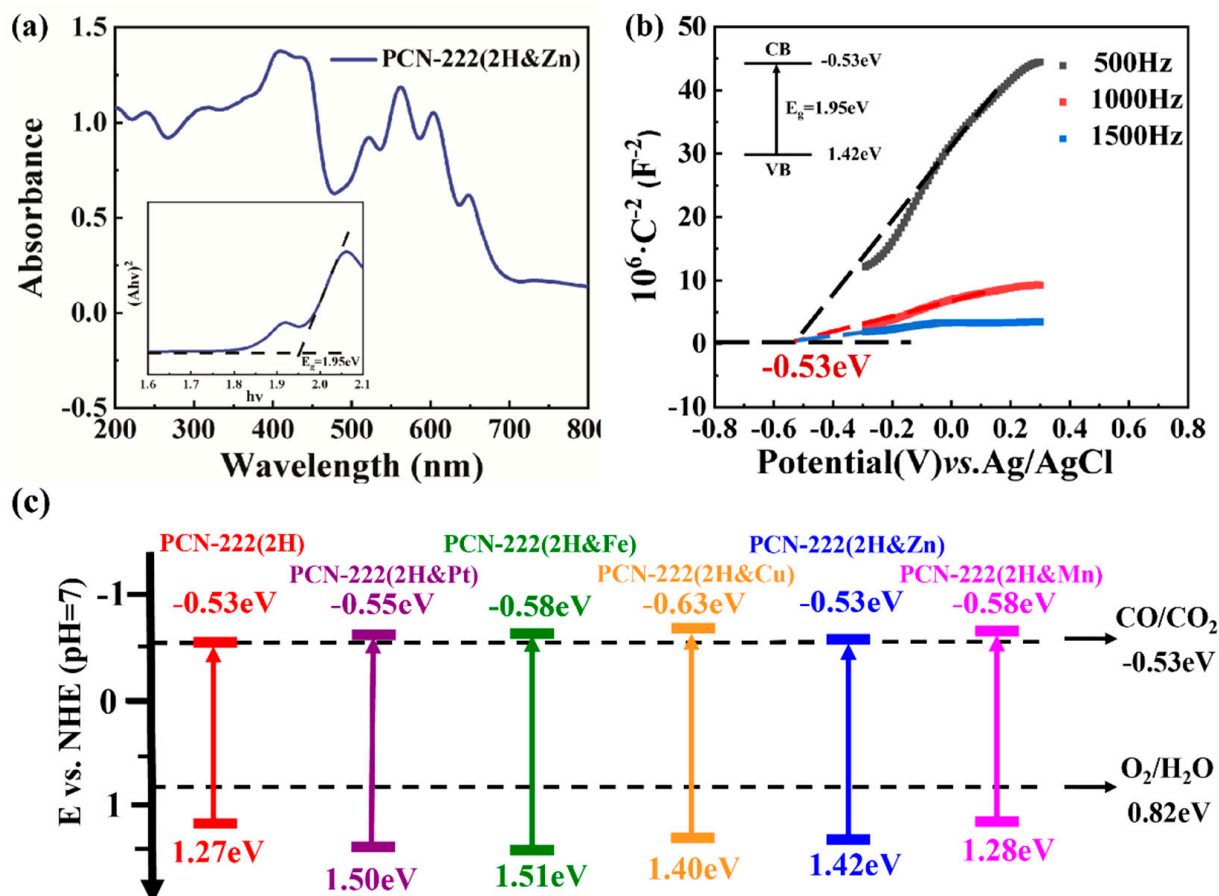


**Figure 4.** (a) UV-vis diffusion spectra and Tauc plot of PCN-222(2H&Zn), (b) Mott-Schottky plots of PCN-222(2H&Zn), and (c) calculated redox potentials of PCN-222(2H) and PCN-222(2H&M).

### 3.2. Photocatalytic CO<sub>2</sub>RR Performance of PCN-222 Materials

Photocatalytic CO<sub>2</sub> reductions using PCN-222(2H&M) as the photocatalysts were tested in a H<sub>2</sub>O medium without using any sacrificial agents and photosensitizers. Figure 5a shows that the average CO yields of PCN-222(2H), PCN-222(2H&Mn), PCN-222(2H&Fe), PCN-222(2H&Pt), PCN-222(2H&Cu), and PCN-222(2H&Zn) were 0.557, 2.77, 3.41, 3.63, 3.64, and 3.92  $\mu\text{mol g}^{-1} \text{h}^{-1}$  under light illumination for 5 h, respectively. In addition, pure PCN-222(Zn) was used as photocatalysts for CO<sub>2</sub>RR, with an average CO yield of 1.36  $\mu\text{mol g}^{-1} \text{h}^{-1}$  (Supporting Information, Figure S4a). Additionally, PCN-222(2H&Zn) with Zn ions at its porphyrin center had the highest photocatalytic CO<sub>2</sub>RR performance among other PCN-222(2H&M) materials, which was seven times and three times higher than that of pure PCN-222(2H) and PCN-222(Zn), respectively. The mass concentration of Zn measured by ICP was 2.6 wt%, which agreed well with the theoretical value of  $\sim 2.7$  wt%. Similarly, it was reported that the effect of porphyrins on photocatalytic activity could be altered by simply altering the degree of metallization [26]. The change in the porphyrin/metalloporphyrin content ratio not only realized the fine-tuning of the photosensitizer/catalyst ratio but also altered the microenvironment surrounding the active site and the charge separation efficiency, confirming the design rationality of PCN-222(2H&Zn)

with both H<sub>2</sub>TCPP and TCPP-Zn, and it was the main factor related to the higher photocatalytic CO<sub>2</sub>RR performance of PCN-222(2H&Zn) compared with pure PCN-222(2H) and PCN-222(Zn). In addition, the activity of PCN-222(2H&Zn) in this work was compared with the literature data (Supporting Information, Table S2). The results show that our PCN-222(2H&Zn) (3.92 μmol g<sup>-1</sup> h<sup>-1</sup>) had higher photocatalytic CO<sub>2</sub> reduction to CO than PCN-222(Cu) (~0.2 μmol g<sup>-1</sup> h<sup>-1</sup>) [41] and PCN-224(Cu) (3.717 μmol g<sup>-1</sup> h<sup>-1</sup>) [42]. At the same time, PCN-222 (5.5 μmol g<sup>-1</sup> h<sup>-1</sup>) [43] displayed higher photocatalytic performance towards the reduction of CO<sub>2</sub> to CO under water vapor conditions, but the PCN-222(2H&Zn) photocatalytic reduction of CO<sub>2</sub> to CO was much more selective than PCN-222 for reduction. To trace the carbon source of the generated CO, the <sup>13</sup>C-isotope labeling experiment was carried out using <sup>13</sup>CO<sub>2</sub> as the reactant. The closed reactor with PCN-222(2H&Zn) dispersed was filled with <sup>13</sup>CO<sub>2</sub>, and the reaction gas was extracted and analyzed by GC-MS after irradiation. As shown in Figure 5b, m/z = 29 and 45 in the mass spectrum corresponded to <sup>13</sup>CO and <sup>13</sup>CO<sub>2</sub>, respectively, which proved that CO was derived from CO<sub>2</sub> photoreduction.

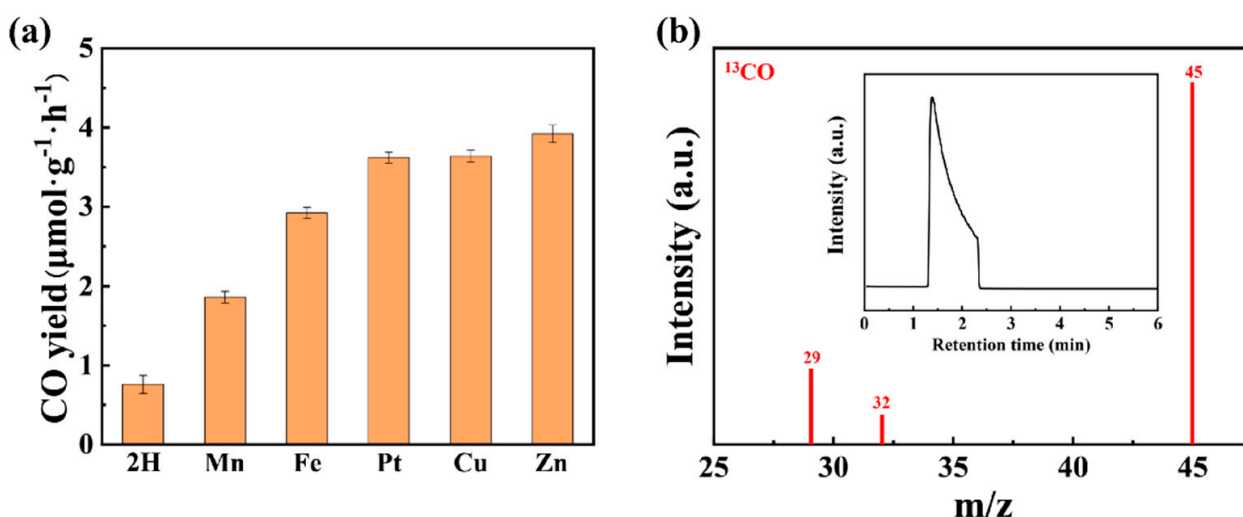


**Figure 5.** (a) The average CO yield of PCN-222(2H), PCN-222(2H&Pt), PCN-222(2H&Fe), PCN-222(2H&Cu), PCN-222(2H&Zn), and PCN-222(2H&Mn). (b) Mass spectra of <sup>13</sup>CO (m/z = 29) produced over PCN-222(2H&Zn) in the photoreduction of <sup>13</sup>CO<sub>2</sub>.

In order to investigate the stability of PCN-222(2H&M), the PXRD profile (Figure 6a) was employed to verify the structures of all PCN-222(2H&M) materials, which could be well-preserved after CO<sub>2</sub>RR. Figure 6b shows that due to the structural stability of PCN-222(2H&Zn), the photocatalytic reactions could be recycled 3 times (5 h per time). Furthermore, three blank tests (without catalysts, without light irradiation, and without CO<sub>2</sub> in N<sub>2</sub> atmosphere) were performed, none of which generated the target product (Figure 6c), confirming the origin of CO during the CO<sub>2</sub>RR process. The photocatalytic CO<sub>2</sub>RR performance of PCN-222(2H&M) materials was significantly improved via the introduction of Zn ions into the porphyrin's center.

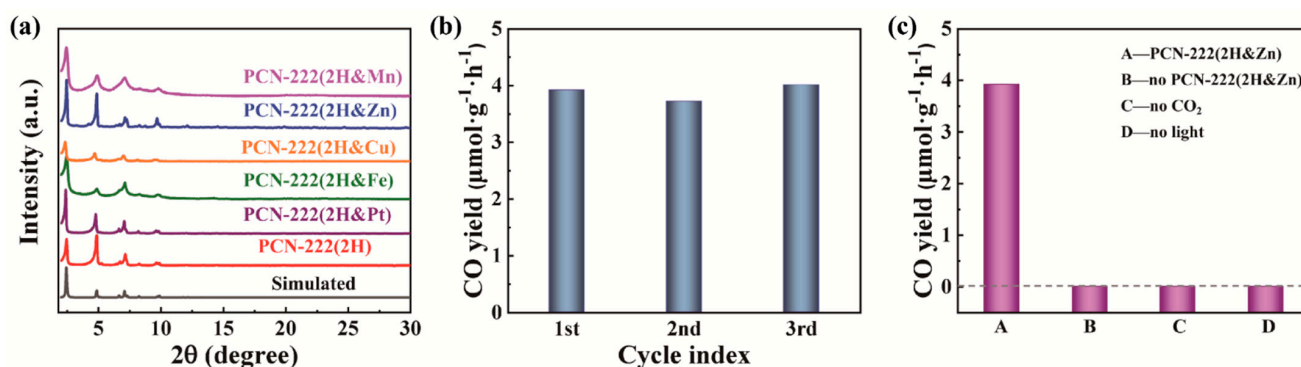


**Figure 6.** (a) PXRD patterns for PCN-222 materials after photocatalytic reactions, (b) the average CO yield of PCN-222(2H&Zn) during the 1st, 2nd, and 3rd photocatalytic CO<sub>2</sub>RR process, respectively; (c) blank tests of CO<sub>2</sub>RR under different conditions (A: normal conditions, B: without PCN-222(2H&Zn), C: without CO<sub>2</sub> in N<sub>2</sub> atmosphere, and D: without light).

### 3.3. Photocatalytic Mechanism Analysis

The photocatalytic activities of various PCN-222 materials were studied using EIS and PL. EIS curves of all PCN-222 materials are shown in Figure 7a and Figure S4b. It was found that all PCN-222(2H&Zn) exhibited smaller semicircles at the high-frequency regime than pure PCN-222(2H), PCN-222(Zn), and other PCN-222(2H&M), demonstrating that the presence of metal ions in the center of metalloporphyrin ligands significantly improved the electron transfer kinetics of PCN-222(2H&M). Moreover, EIS curves of PCN-222(2H&Zn) showed the smallest semicircle diameter compared with the other PCN-222(2H&M), illustrating the significance of Zn ions for promoting the reduced resistance of PCN-222(2H&M).

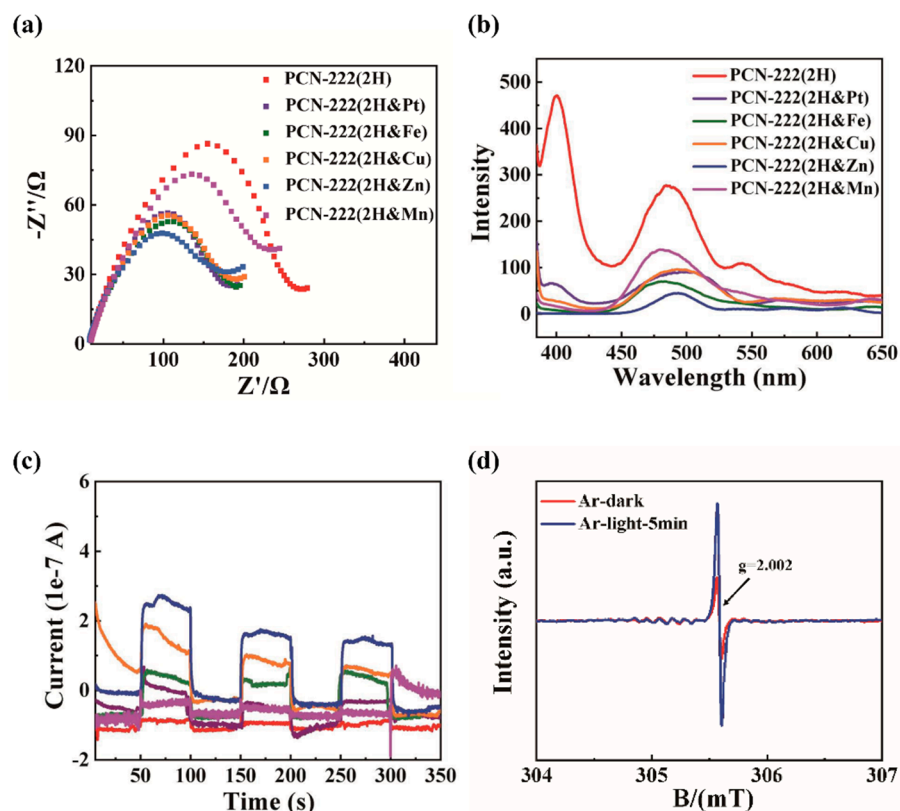


**Figure 7.** (a) EIS and (b) solid-state PL spectra excited at  $\lambda = 350$  nm, (c) transient photocurrents of PCN-222(2H) and PCN-222(2H&M), and (d) EPR of PCN-222(2H&Zn).

It is known that after the catalyst is photoexcited, photogenerated electrons and holes are produced, and fluorescence occurs when these electrons and holes are combined. Hence, the photocatalyst's electron and hole separation efficiency can be accurately represented by the fluorescence intensity [37]. According to PL spectra of PCN-222 materials (Figure 7b and Figure S4c), the presence of metal ions in the center of the metalloporphyrin ligands decreased their photoluminescence intensities. PCN-222(2H&Zn) exhibited a lower rate of electron–hole complexation than pure PCN-222(2H), PCN-222(Zn) and other PCN-222(2H&M) due to the lowest fluorescence intensity of PCN-222(2H&Zn). The photocurrent responses of all PCN-222 materials are shown in Figure 7c. Compared with other PCN-222(2H&M) materials, PCN-222(2H&Zn) showed a higher current density, suggesting the highest electron separation and transport efficiency under light irradiation. Additionally, the excellent photocatalytic activity of PCN-222(2H&Zn) was attributed to its high separation efficiency of the photoinduced charges. To further unveil the charge transfer behavior in CO<sub>2</sub> photoreduction over PCN-222(2H&M), the electron paramagnetic resonance (EPR) analysis was performed. To explore the charge transfer behavior during the photocatalytic CO<sub>2</sub> reaction over PCN-222(2H&Zn), EPR measurements were conducted. As shown in Figure 7d, the EPR peak of PCN-222(2H&Zn) at  $g = 2.002$  was attributed to the generation of Zr(III) from Zr(IV), suggesting the charge transfer from organic ligands to Zr clusters in PCN-222(2H&Zn) [44,45]. In addition, under the condition of an Ar atmosphere, the EPR peak intensity of PCN-222(2H&Zn) was higher in the presence of light compared with in darkness, signifying the generation of more Zr(III) in light.

Metal sites of MOFs can improve their CO<sub>2</sub> capture capability and photocatalytic activity due to the role of active sites toward CO<sub>2</sub> adsorption [46]. Based on the above results, we proposed a possible reaction mechanism (Figure 8). TCPP-M linkers in PCN-222(2H&M) behaved as antennas to absorb visible light, promoting an excited state for the transfer of electrons to Zr clusters. Then, Zr(IV) in the clusters was reduced to Zr(III), which reduced CO<sub>2</sub> to CO. Additionally, the presence of transition metals in porphyrin ligands improved the efficiency of these reactions, which was consistent with decreased PL and the EIS intensity of PCN-222(2H&M). Furthermore, the valence transition from Zr(IV) in Zr-O clusters to Zr(III) was the key factor in the reduction of CO<sub>2</sub> to CO.

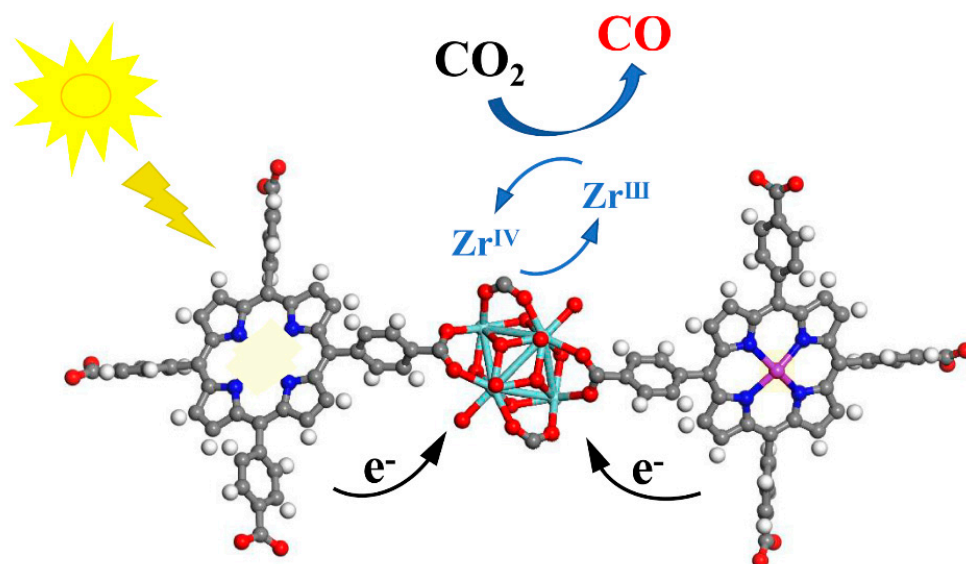


**Figure 8.** Proposed mechanism for the photocatalytic CO<sub>2</sub> reduction over PCN-222(2H&M).

#### 4. Conclusions

In this work, the effect of various central metal ions of PCN-222(2H&M) on photocatalytic CO<sub>2</sub> reduction performance was investigated using water as the oxidant under light-irradiated conditions in the absence of any organic solvent and sacrificial agent. Ac-

According to EIS and PL, the introduction of porphyrin-centered metal ions significantly improved their photocatalytic activity for CO<sub>2</sub> reduction. Furthermore, PCN-222(2H&Zn) showed the highest photocatalytic CO<sub>2</sub>RR performance, with an average CO yield of 3.92 μmol g<sup>-1</sup> h<sup>-1</sup> in the absence of any organic solvent and sacrificial agent, which was seven times higher than that of PCN-222(2H) (0.557 μmol g<sup>-1</sup> h<sup>-1</sup>). Therefore, this work provides a novel pathway to improve the photocatalytic reduction activity of porphyrin-based MOFs and further clarifies the role of transition metal ions in porphyrin centers for effectively reducing electron and hole recombination rates.

**Supplementary Materials:** The following supporting information can be downloaded at: <https://www.mdpi.com/article/10.3390/pr11041042/s1>, Figure S1: EDX-mapping images of (a) PCN-222(2H), (b) PCN-222(2H&Pt), (c) PCN-222(2H&Fe), (d) PCN-222(2H&Cu), (e) PCN-222(2H&Zn) and (f) PCN-222(2H&Mn), respectively.; Figure S2: TGA curves of PCN-222(2H) and PCN-222(2H&M); Figure S3: (a) UV-vis diffusion spectra and Tauc plot of PCN-222(2H), (b) Mott-Schottky plots of PCN-222(2H), (c) UV-vis diffusion spectra and Tauc plot of PCN-222(2H&Pt), (d) Mott-Schottky plots of PCN-222(2H&Pt), (e) UV-vis diffusion spectra and Tauc plot of PCN-222(2H&Fe), (f) Mott-Schottky plots of PCN-222(2H&Fe), (g) UV-vis diffusion spectra and Tauc plot of PCN-222(2H&Cu), (h) Mott-Schottky plots of PCN-222(2H&Cu), (i) UV-vis diffusion spectra and Tauc plot of PCN-222(2H&Mn), and (j) Mott-Schottky plots of PCN-222(2H&Mn); Figure S4: (a) The average CO yield, (b) EIS and (c) solid-state PL spectra excited at λ = 350 nm of PCN-222(2H), PCN-222(2H&Zn) and PCN-222(Zn); Table S1: Structural characteristics of PCN-222 materials; Table S2: Summary of photocatalytic CO<sub>2</sub> reduction performances of porphyrin-based MOFs materials in water or water vapor without the use of any organic solvent, photosensitizer, and sacrificial reagent.

**Author Contributions:** Conceptualization, Y.S.; methodology, K.W.; software, Q.L. (Qian Li) and Q.W.; validation, Q.L. (Qian Li), M.Z., and Y.L.; formal analysis, K.W.; investigation, Q.L. (Qian Li), M.Z., and Q.L. (Qiang Li); resources, Y.S.; data curation, Q.L. (Qian Li), H.W., and B.Z.; writing—original draft preparation, Q.L. (Qian Li); writing—review and editing, K.W.; supervision, K.W. and H.-M.S.; project administration, K.W. and Y.S.; funding acquisition, K.W. and Y.S. All authors have read and agreed to the published version of the manuscript.

**Funding:** This research was funded by the National Natural Science Foundation of China (22138011, 21808201, 21905248) and Zhejiang Provincial Natural Science Foundation of China (LY22B060006) for financial support.

**Acknowledgments:** The authors acknowledge the financial support from the National Natural Science Foundation of China (22138011, 21808201, 21905248) and Zhejiang Provincial Natural Science Foundation of China (LY22B060006).

**Conflicts of Interest:** The authors declare no conflict of interest.

## References

1. Song, J.; Lu, Y.; Lin, Y.; Liu, Q.; Wang, X.; Su, W. A direct Z-scheme α-Fe<sub>2</sub>O<sub>3</sub>/LaTiO<sub>2</sub>N visible-light photocatalyst for enhanced CO<sub>2</sub> reduction activity. *Appl. Catal. B Environ.* **2021**, *292*, 120185. [CrossRef]
2. Li, X.; Liu, H.; Luo, D.; Li, J.; Huang, Y.; Li, H.; Fang, Y.; Xu, Y.; Zhu, L. Adsorption of CO<sub>2</sub> on heterostructure CdS(Bi<sub>2</sub>S<sub>3</sub>)/TiO<sub>2</sub> nanotube photocatalysts and their photocatalytic activities in the reduction of CO<sub>2</sub> to methanol under visible light irradiation. *Chem. Eng. J.* **2012**, *180*, 151. [CrossRef]
3. Hiragond, C.; Ali, S.; Sorcar, S.; In, S. Hierarchical Nanostructured Photocatalysts for CO<sub>2</sub> Photoreduction. *Catalysts* **2019**, *9*, 370. [CrossRef]
4. Wang, K.; Cao, M.; Lu, J.; Lu, Y.; Lau, C.H.; Zheng, Y.; Fan, X. Operando DRIFTS-MS investigation on plasmon-thermal coupling mechanism of CO<sub>2</sub> hydrogenation on Au/TiO<sub>2</sub>: The enhanced generation of oxygen vacancies. *Appl. Catal. B Environ.* **2021**, *296*, 120341. [CrossRef]
5. Karmakar, S.; Barman, S.; Rahimi, F.A.; Maji, T.K. Covalent grafting of molecular photosensitizer and catalyst on MOF-808: Effect of pore confinement toward visible light-driven CO<sub>2</sub> reduction in water. *Energy Environ. Sci.* **2021**, *14*, 2429–2440. [CrossRef]
6. Wang, G.; Chen, J.; Ding, Y.; Cai, P.; Yi, L.; Li, Y.; Tu, C.; Hou, Y.; Wen, Z.; Dai, L. Electrocatalysis for CO<sub>2</sub> conversion: From fundamentals to value-added products. *Chem. Soc. Rev.* **2021**, *50*, 4993. [CrossRef]
7. Jiang, X.; Nie, X.; Guo, X.; Song, C.; Chen, J.G. Recent Advances in Carbon Dioxide Hydrogenation to Methanol via Heterogeneous Catalysis. *Chem. Rev.* **2020**, *120*, 7984–8034. [CrossRef]

8. Alshorifi, F.T.; Alswat, A.A.; Mannaa, M.A.; Alotaibi, M.T.; El-Bahy, S.M.; Salama, R.S. Facile and Green Synthesis of Silver Quantum Dots Immobilized onto a Polymeric CTS-PEO Blend for the Photocatalytic Degradation of p-Nitrophenol. *ACS Omega* **2021**, *6*, 30432–30441. [[CrossRef](#)]
9. Alshorifi, F.T.; Ali, S.L.; Salama, R.S. Promotional Synergistic Effect of Cs–Au NPs on the Performance of Cs–Au/MgFe<sub>2</sub>O<sub>4</sub> Catalysts in Catalysis 3,4-Dihydropyrimidin-2(1H)-Ones and Degradation of RhB Dye. *J. Inorg. Organomet. Polym. Mater.* **2022**, *32*, 3765–3776. [[CrossRef](#)]
10. Alshorifi, F.T.; Alswat, A.A.; Salama, R.S. Gold-selenide quantum dots supported onto cesium ferrite nanocomposites for the efficient degradation of rhodamine B. *Heliyon* **2022**, *8*, e09652. [[CrossRef](#)]
11. Lei, Z.; Xue, Y.; Chen, W.; Qiu, W.; Zhang, Y.; Horike, S.; Tang, L. MOFs-Based Heterogeneous Catalysts: New Opportunities for Energy-Related CO<sub>2</sub> Conversion. *Adv. Energy Mater.* **2018**, *8*, 1801587. [[CrossRef](#)]
12. Zhang, Z.; Zhu, Y.; Chen, X.; Zhang, H.; Wang, J. A Full-Spectrum Metal-Free Porphyrin Supramolecular Photocatalyst for Dual Functions of Highly Efficient Hydrogen and Oxygen Evolution. *Adv. Mater.* **2019**, *31*, 1806626. [[CrossRef](#)]
13. Taniguchi, M.; Lindsey, J.S. Synthetic Chlorins, Possible Surrogates for Chlorophylls, Prepared by Derivatization of Porphyrins. *Chem. Rev.* **2017**, *117*, 344–535. [[CrossRef](#)]
14. Li, J.; Zhao, Y.; Wang, X.; Wang, T.; Hou, X. Rapid microwave synthesis of PCN-134-2D for singlet oxygen based-oxidative degradation of ranitidine under visible light: Mechanism and toxicity assessment. *Chem. Eng. J.* **2022**, *443*, 136424. [[CrossRef](#)]
15. Leng, F.; Liu, H.; Ding, M.; Lin, Q.; Jiang, H. Boosting Photocatalytic Hydrogen Production of Porphyrinic MOFs: The Metal Location in Metalloporphyrin Matters. *ACS Catal.* **2018**, *8*, 4583–4590. [[CrossRef](#)]
16. Li, P.; Zhang, X.; Hou, C.; Chen, Y.; He, T. Highly efficient visible-light driven solar-fuel production over tetra(4-carboxyphenyl)porphyrin iron (III) chloride using CdS/Bi<sub>2</sub>S<sub>3</sub> heterostructure as photosensitizer. *Appl. Catal. B Environ.* **2018**, *238*, 656–663. [[CrossRef](#)]
17. Wang, L.; Jin, P.; Duan, S.; She, H.; Huang, J.; Wang, Q. In-situ incorporation of Copper(II) porphyrin functionalized zirconium MOF and TiO<sub>2</sub> for efficient photocatalytic CO<sub>2</sub> reduction. *Sci. Bull.* **2019**, *64*, 926–933. [[CrossRef](#)]
18. Wang, Z.; Jiao, X.; Chen, D.; Li, C.; Zhang, M. Porous Copper/Zinc Bimetallic Oxides Derived from MOFs for Efficient Photocatalytic Reduction of CO<sub>2</sub> to Methanol. *Catalysts* **2020**, *10*, 1127. [[CrossRef](#)]
19. Credico, B.D.; Redaelli, M.; Bellardita, M.; Calamante, M.; Cepek, C.; Cobani, E.; D’Arienzo, M.; Evangelisti, C.; Marelli, M.; Moret, M.; et al. Step-by-Step Growth of HKUST-1 on Functionalized TiO<sub>2</sub> Surface: An Efficient Material for CO<sub>2</sub> Capture and Solar Photoreduction. *Catalysts* **2018**, *8*, 353. [[CrossRef](#)]
20. Kitao, T.; Zhang, Y.; Kitagawa, S.; Wang, B.; Uemura, T. Hybridization of MOFs and polymers. *Chem. Soc. Rev.* **2017**, *46*, 3108. [[CrossRef](#)]
21. Zhao, T.; Wu, H.; Wen, X.; Zhang, J.; Tang, H.; Deng, Y.; Liao, S.; Tian, X. Recent advances in MOFs/MOF derived nanomaterials toward high-efficiency aqueous zinc ion batteries. *Coord. Chem. Rev.* **2022**, *468*, 214642. [[CrossRef](#)]
22. Gao, X.; Liu, B.; Zhao, X. Thiol-decorated defective metal-organic framework for effective removal of mercury(II) ion. *Chemosphere* **2023**, *317*, 137891. [[CrossRef](#)] [[PubMed](#)]
23. Gong, X.; Noh, H.; Gianneschi, N.C.; Farha, O.K. Interrogating Kinetic versus Thermodynamic Topologies of Metal-organic frameworks via Combined Transmission Electron Microscopy and X-ray Diffraction Analysis. *J. Am. Chem. Soc.* **2019**, *141*, 6146–6151. [[CrossRef](#)] [[PubMed](#)]
24. Sarker, M.; Shin, S.; Jeong, J.H.; Jung, S.H. Mesoporous metal-organic framework PCN-222(Fe): Promising adsorbent for removal of big anionic and cationic dyes from water. *Chem. Eng. J.* **2019**, *371*, 252–259. [[CrossRef](#)]
25. Xu, H.; Hu, J.; Wang, D.; Li, Z.; Zhang, Q.; Luo, Y.; Yu, S.; Jiang, H. Visible-Light Photoreduction of CO<sub>2</sub> in a Metal-Organic Framework: Boosting Electron-Hole Separation via Electron Trap States. *J. Am. Chem. Soc.* **2015**, *137*, 13440–13443. [[CrossRef](#)]
26. Zhang, A.; Si, D.; Huang, H.; Xie, L.; Fang, Z.; Liu, T.; Cao, R. Partial Metalation of Porphyrin Moieties in Hydrogen-Bonded Organic Frameworks Provides Enhanced CO<sub>2</sub> Photoreduction Activity. *Angew. Chem. Int. Ed.* **2022**, *61*, e202203955.
27. Jin, J. Highly stable and efficient visible-light-driven carbon dioxide reduction by zirconium-metalloporphyrin PCN-222 via dual catalytic routes. *React. Kinet. Mech. Catal.* **2020**, *131*, 397–408. [[CrossRef](#)]
28. Moghaddam, Z.S.; Kaykhani, M.; Khajeh, M.; Oveisi, A.R. PCN-222 metal-organic framework: A selective and highly efficient sorbent for the extraction of aspartame from gum, juice, and diet soft drink before its spectrophotometric determination. *BMC Chem.* **2020**, *14*, 19. [[CrossRef](#)]
29. Guo, Y.; Zhang, X.; Xie, N.; Guo, R.; Wang, Y.; Sun, Z.; Li, H.; Jia, H.; Niu, D.; Sun, H. Investigation of antimony adsorption on a zirconium-porphyrin-based metal-organic framework. *Dalton Trans.* **2021**, *50*, 13932. [[CrossRef](#)]
30. Hariri, R.; Dehghanpour, S. Adsorptive removal and visible-light photocatalytic degradation of large cationic and anionic dyes induced by air-bubbles in the presence of a magnetic porphyrinic metal-organic framework (Fe<sub>3</sub>O<sub>4</sub>@SiO<sub>2</sub>@PCN-222 (Fe)). *J. Phys. Chem. Solids* **2021**, *155*, 110126. [[CrossRef](#)]
31. Gao, L.; Hu, X.; Qin, S.; Chu, H.; Zhao, X.; Wang, B. L-Cysteine modified metal-organic framework as a chiral stationary phase for enantioseparation by capillary electrochromatography. *RSC Adv.* **2022**, *12*, 6063–6075.
32. Wang, R.; Fan, Y.; Wang, L.; Wu, L.; Sun, S.; Sun, S. Pt nanocatalysts on a polyindole-functionalized carbon nanotube composite with high performance for methanol electrooxidation. *J. Power Sources* **2015**, *287*, 341–348. [[CrossRef](#)]
33. Han, B.; Yu, S.; Wang, Z.; Zhu, H. Imidazole polymerized ionic liquid as a precursor for an iron-nitrogen-doped carbon electrocatalyst used in the oxygen reduction reaction. *Int. J. Hydrog. Energy* **2020**, *45*, 29645–29654. [[CrossRef](#)]

34. Huang, G.; Su, T.; Zeng, K.; Guo, Y.; Zhao, S.; Wei, S. Mesoporous chitosan-immobilized iron tetrakis(4-carboxyphenyl)porphyrin as a model of cytochrome P-450 enzyme for oxidation of ethylbenzene. *Appl. Organomet. Chem.* **2018**, *32*, e4140. [[CrossRef](#)]
35. Chung, N.T.K.; Dang, H.P.; Nguyen, T.P.; Le, T. Effects of Zn and Zn-N doping on optical, electrical, and structural properties of p-type SnO<sub>2</sub> films. *J. Photochem. Photobiol. A Chem.* **2021**, *418*, 113436. [[CrossRef](#)]
36. Zhang, Y.; Zhang, Y.; Huang, Y.; Jia, Y.; Chen, L.; Pan, Y.; Wang, M. Adsorptive-photocatalytic performance and mechanism of Me (Mn, Fe)-N co-doped TiO<sub>2</sub>/SiO<sub>2</sub> in cyanide wastewater. *J. Alloy. Compd.* **2021**, *867*, 159020. [[CrossRef](#)]
37. Shi, L.; Yang, L.; Zhang, H.; Chang, K.; Zhao, G.; Kako, T.; Ye, J. Implantation of Iron (III) in Porphyrinic Metal Organic Frameworks for Highly Improved Photocatalytic Performance. *Appl. Catal. B Environ.* **2018**, *224*, 60–68. [[CrossRef](#)]
38. Liu, D.; Cai, W.; Wang, Y.; Zhu, Y. Constructing a novel Bi<sub>2</sub>SiO<sub>5</sub>/BiPO<sub>4</sub> heterostructure with extended light response range and enhanced photocatalytic performance. *Appl. Catal. B Environ.* **2018**, *236*, 205–211. [[CrossRef](#)]
39. Qin, J.; Xiao, Z.; Xu, P.; Li, Z.; Lu, X.; Yang, X.; Lu, W.; Ma, L.; Li, D. Anionic Porous Zn-Metalated Porphyrin Metal-Organic Framework with PtS Topology for Gas-Phase Photocatalytic CO<sub>2</sub> Reduction. *Inorg. Chem.* **2022**, *61*, 13234–13238. [[CrossRef](#)]
40. Jin, J. Porphyrin-based metal-organic framework catalysts for photoreduction of CO<sub>2</sub>: Understanding the effect of node connectivity and linker metalation on activity. *New J. Chem.* **2020**, *44*, 15362. [[CrossRef](#)]
41. Duan, S.; Wu, S.; Wang, L.; She, H.; Huang, J.; Wang, Q. Rod-Shaped Metal Organic Framework Structured PCN-222(Cu)/TiO<sub>2</sub> Composites for Efficient Photocatalytic CO<sub>2</sub> Reduction. *Wuli Huaxue Xuebao* **2020**, *36*, 19050861–19050868.
42. Wang, L.; Jin, P.; Huang, J.; She, H.; Wang, Q. Integration of Copper(II)-Porphyrin Zirconium Metal-Organic Framework and Titanium Dioxide to Construct Z-Scheme System for Highly Improved Photocatalytic CO<sub>2</sub> Reduction. *ACS Sustain. Chem. Eng.* **2019**, *7*, 15660. [[CrossRef](#)]
43. Fang, Z.; Liu, T.; Liu, J.; Jin, S.; Wu, X.; Gong, X.; Wang, K.; Yin, Q.; Liu, T.; Gao, R.; et al. Boosting Interfacial Charge-Transfer Kinetics for Efficient Overall CO<sub>2</sub> Photoreduction via Rational Design of Coordination Spheres on Metal-Organic Frameworks. *J. Am. Chem. Soc.* **2020**, *142*, 12515. [[CrossRef](#)]
44. Sun, D.; Fu, Y.; Liu, W.; Ye, L.; Wang, D.; Yang, L.; Fu, X.; Li, Z. Studies on Photocatalytic CO<sub>2</sub> Reduction over NH<sub>2</sub>-UiO-66(Zr) and Its Derivatives: Towards a Better Understanding of Photocatalysis on Metal-organic frameworks. *Chem. Eur. J.* **2013**, *19*, 14279. [[CrossRef](#)] [[PubMed](#)]
45. Li, J.; Huang, H.; Xue, W.; Sun, K.; Song, X.; Wu, C.; Nie, L.; Li, Y.; Liu, C.; Pan, Y.; et al. Self-adaptive dual-metal-site pairs in metal-organic frameworks for selective CO<sub>2</sub> photoreduction to CH<sub>4</sub>. *Nat. Catal.* **2021**, *4*, 719. [[CrossRef](#)]
46. Hariri, R.; Dehghanpour, S. Effective visible-light CO<sub>2</sub> photoreduction over (metallo) porphyrin-based metal-organic frameworks to achieve useful hydrocarbons. *Appl. Organomet. Chem.* **2021**, *35*, e6422. [[CrossRef](#)]

**Disclaimer/Publisher's Note:** The statements, opinions and data contained in all publications are solely those of the individual author(s) and contributor(s) and not of MDPI and/or the editor(s). MDPI and/or the editor(s) disclaim responsibility for any injury to people or property resulting from any ideas, methods, instructions or products referred to in the content.